Dalton Transactions

# $d_{z^2}$ Orbital character of polyhedra in complex solid-state transition-metal compounds



| | |
|---|---|
| Journal: | *Dalton Transactions* |
| Manuscript ID | DT-ART-10-2019-004091.R2 |
| Article Type: | Paper |
| Date Submitted by the Author: | 07-Dec-2019 |
| Complete List of Authors: | Ohkubo, Isao; National Institute for Materials Science (NIMS), Center for Functional Sensor & Actuator, Research Center for Functional Materials<br>Mori, Takao; National Institute for Materials Science, |
| | |

Dalton Transactions

PAPER

# $d_z^2$ Orbital character of polyhedra in complex solid-state transition-metal compounds

Received 00th January 2019,
Accepted 00th January 20xx

DOI: 10.1039/x0xx00000x

Isao Ohkubo*[a,b,c] and Takao Mori[a,b]

In transition-metal compounds, the character of the d orbitals often plays an important role in the development and enhancement of novel physical and chemical properties. Density functional theory calculations of the electronic structures of various $d^0$ and $d^1$ complex transition-metal compounds consisting of either face-sharing octahedra, edge-sharing octahedra, or edge-sharing trigonal prismatic layers were performed to investigate the nature of their d orbitals. The $d_z^2$ orbital of the transition metal was shown to make a significant contribution to the electronic structure near the Fermi level in nine different complex transition-metal compounds (oxides, nitrides, and sulfides), regardless of the type of polyhedral geometry and connectivity. The importance of controlling and designing the $d_z^2$ orbital character of transition metals near the Fermi level was shown to be important in developing novel physical and chemical properties in complex transition-metal compounds.

## Introduction

Complex transition-metal compounds display a rich variety of physical and chemical properties. In ionic transition-metal compounds such as oxides, nitrides, pnictides, or chalcogenides, including monolayered dichalcogenides, the d orbitals often play important roles in determining the electronic structure near the Fermi level. As a result, such compounds exhibit a range of unique physical and chemical properties, such as superconductivity,[1–4] magnetism,[5,6] thermoelectric transport properties,[7] high-electron-mobility semiconductivity,[8,9] anomalous metallic/semimetallic states,[10] electrocatalytic oxygen-evolution reactions,[11] or catalytic activity for various chemical reactions.[12] According to crystal field theory, the energy levels of d orbitals are split as a result of interactions between positively charged transition-metal cations and negatively charged anions. Splitting of d orbital energy levels in the crystal fields is influenced by the type of transition-metal cation, the nature of the anion, the coordination number of the transition metal, and the local atomic structure.[13] Among various types of hexacoordinate polyhedra, the crystal fields of face- and edge-sharing octahedra and trigonal prismatic layers lead to the formation of an energy level of a singlet $d_z^2$ ($a_{1g}$ or $a_1$ or $a_2$) orbital and a tendency to form an electron band mainly from contributions from $d_z^2$ orbitals near the Fermi level in ionic complex transition-metal compounds. The $d_z^2$ orbital frequently plays vital role in the manifestation of novel physical and chemical properties.[11,12,14–20] In comparison with d orbital characters of transition metals in corner-sharing octahedra, the d orbital characters in face- and edge-sharing octahedra and in edge-sharing trigonal prismatic layers are less well understood.

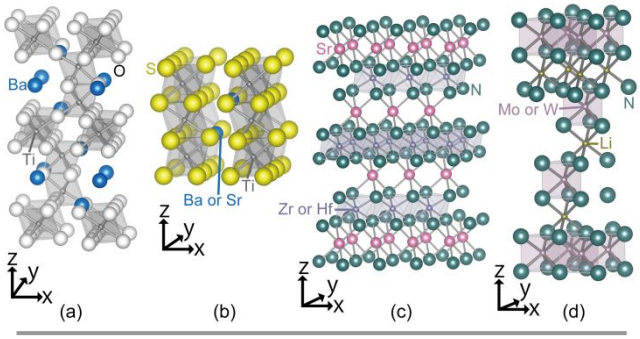


**Figure 1.** Crystal structures of (a) 4H-hexagonal perovskite $BaTiO_3$ and (b) 2H-hexagonal perovskite $ATiS_3$ (A = Ba, Sr), consisting of face-sharing octahedral blocks, (c) $\alpha$-$NaFeO_2$-type $AMN_2$ (A = Na, Sr; M = Nb, Ta, Zr, Hf) composed of edge-sharing $MN_6$ octahedral layers, and (d) $LiMN_2$ (M = Mo, W) consisting of $MN_6$ edge-sharing trigonal prismatic layers.

The present study focused on $d^0$- and $d^1$-complex transition-metal oxides, nitrides, and sulfides with the chemical formula $AMX_3$ or $AMX_2$ (where A is a cation of an alkali metal or an alkaline earth metal, M is a transition-metal ion, and X = O, N, or S) containing various types of polyhedra, as shown in Figure 1. The 4H-type hexagonal perovskite $BaTiO_3$ ($d^0$) contains two $TiO_6$ octahedra connected by a common face.[21] The 2H-type hexagonal perovskites $BaTiS_3$[22] and $SrTiS_3$[23] contain quasi-one-dimensional chains of face-sharing $TiS_6$ octahedra that are separated by chains of A-site cations; both are $d^0$ transition-

[a] Center for Functional Sensor & Actuator (CFSN), Research Center for Functional Materials, National Institute for Materials Science (NIMS), 1-1 Namiki, Tsukuba, Ibaraki 305-0044, Japan. E-mail: OHKUBO.Isao@nims.go.jp
[b] International Center for Materials Nanoarchitectonics (MANA), National Institute for Materials Science (NIMS), 1-1 Namiki, Tsukuba, Ibaraki 305-0044, Japan
[c] Center for Materials Research by Information Integration (CMI²), Research and Services Division of Materials Data and Integrated System (MaDIS), National Institute for Materials Science (NIMS), 1-1 Namiki, Tsukuba, Ibaraki 305-0044, Japan

Electronic Supplementary Information (ESI) available: [Computational details; electronic structures of 2H-type hexagonal perovskite $SrTiS_3$, $SrHfN_2$, and $LiWN_2$.]. See DOI: 10.1039/x0xx00000x

metal sulfides. $SrZrN_2$,[24] $SrHfN_2$,[24] $NaNbN_2$,[25] and $NaTaN_2$[26] are $\alpha$-$NaFeO_2$-type $d^0$-layered complex metal nitrides that have edge-sharing $MN_6$ (M = Zr, Hf, Nb, Ta) octahedral layers along the *c*-axis. The $d^1$-complex transition-metal nitrides $LiMoN_2$[27] and $LiWN_2$[28] also have layered crystal structures composed of alternately stacked $MoN_6$ or $WN_6$ edge-sharing trigonal prismatic layers and $LiN_6$ octahedral layers. Structural coordinates of these trigonal prismatic layers are equivalent to those of monolayer dichalcogenides, such as $MoS_2$, $WSe_2$, or $WTe_2$.[18,19,29] To investigate the effects of the polyhedra on the character of the d-orbitals in these complex transition-metal compounds containing various types of polyhedra, we calculated their electronic structures by means of density functional theory (DFT) methods.

## Computational Methods

Our electronic structure calculations were performed by applying DFT through a full-potential linearized augmented plane-wave approach implemented in WIEN2k code.[30] We used two types of exchange-correlation potential/functional: the modified Becke–Johnson (mBJ) exchange potential[31,32] and the generalized gradient approximation Perdew–Burke–Ernzerhof (GGA-PBE) functional.[33,34] A GGA-PBE+*U* approach was also adopted, in which *U* is the effective on-site Coulomb interaction correction. The parameter $R_{mt}K_{max}$, in which $K_{max}$ is the plane-wave cutoff and $R_{mt}$ is the smallest muffin-tin radius, was used to control the size of the basis set: this parameter was set to a high value of 7.0 for all compounds. A total of 100 ***k***-points in the Brillouin zone were used to calculate the electronic structure. Convergences were reached with ***k***-point sampling of 100. Structural coordinates and lattice parameters of the compounds obtained by neutron or X-ray diffraction measurements were used in the DFT calculations.[21–28] The crystal structures were visualized with the VESTA code.[35] More details of the calculation conditions can be found in the Electronic Supplementary Information (ESI).

## Results and discussion

### Face-sharing octahedra in $d^0$ hexagonal perovskites $ATiX_3$ (A = Sr or Ba; X = O or S)

Hexagonal perovskite compounds generally display tolerance factors[36] of >1, indicating that cubic close packing is geometrically frustrated. Several types of hexagonal perovskite polymorphs have been reported.[5] Among hexagonal perovskite compounds, the 9L-type hexagonal perovskite $BaRuO_3$[37] and the 2H-type hexagonal perovskite $BaVS_3$[38,39] display interesting metal–insulator transitions. The 18R-type hexagonal perovskite $BaIrO_3$ shows an electronic phase transition between a ferromagnetic Mott insulator state and a paramagnetic charge-ordered insulator state.[40] The 4H-type hexagonal perovskite $BaTiO_3$ displays a large dielectric constant and ferroelectricity.[41,42] The chalcogenide perovskites $AMX_3$ (A = Ca, Sr, Ba; M = Ti, Zr, Hf; X = S, Se), which contain hexagonal and needle-like phases, have recently attracted attention as photovoltaic materials.[43] Among the various hexagonal perovskites, we focused on 4H-$BaTiO_3$ ($Ti^{4+}$; $d^0$) and 2H-$ATiS_3$ (A = $Sr^{2+}$, $Ba^{2+}$, $Ti^{4+}$; $d^0$) in this study, because these compounds contain relatively simple face-sharing octahedral blocks (Figures 1a and 1b).

The electronic structure of the 4H-type hexagonal perovskite $BaTiO_3$, as calculated from the mBJ exchange potential, is shown in Figures 2 and 3. 4H-$BaTiO_3$ is a band insulator with a direct energy band gap of 2.72 eV at the Γ-point; its experimentally determined band gap is 3.25 eV.[44] The

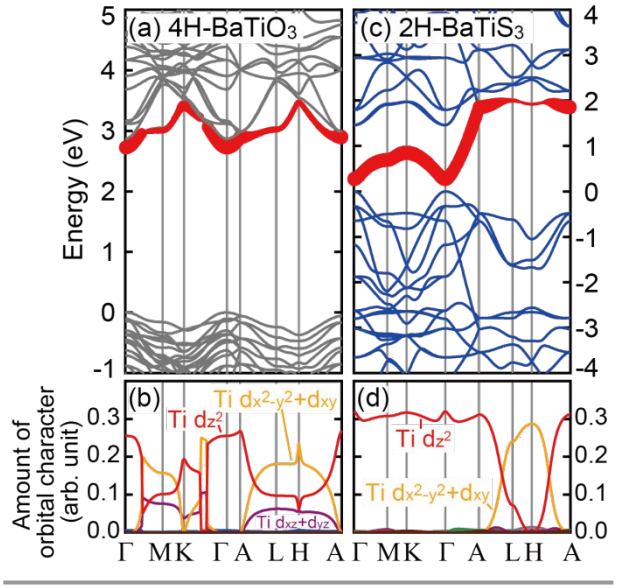


**Figure 2.** Electronic band structures and orbital characters for the lowest conduction bands in 4H-hexagonal perovskite $BaTiO_3$ and 2H-$BaTiS_3$. (a) and (c) electronic band structures of 4H-$BaTiO_3$ and 2H-$BaTiS_3$, respectively. The amount of Ti $3d_{z^2}$ orbital character is depicted in the lowest conduction bands by the width of the lines, revealing that the lowest conduction bands have a strong Ti $3d_{z^2}$ orbital characters in 4H-$BaTiO_3$ and 2H-$BaTiS_3$. These electronic band structures were calculated by the mBJ exchange potential for 4H-$BaTiO_3$ and by the GGA-PBE+*U* method for 2H-$BaTiS_3$ ($U_{eff}$ = 8 eV). (b) and (d) orbital characters for the lowest conduction bands of 4H-$BaTiO_3$ and 2H-$BaTiS_3$, respectively. All s orbitals, p orbitals ($p_z$, $p_x + p_y$ for Ba and Ti; $p_x$, $p_y$, $p_z$ for O and S), and d orbitals ($d_{z^2}$, $d_{x^2-y^2} + d_{xy}$, $d_{xz} + d_{yz}$ for Ba and Ti) are plotted in Figures 4b and 4c.

value of the energy band gap in 4H-$BaTiO_3$ calculated from the mBJ exchange potential agrees much more closely with the experimental value than does the energy band gap of 1.90 eV calculated by means of the GGA-PBE functional (not shown). The energies at the Fermi level are set to 0 eV. The highest valence band in 4H-$BaTiO_3$ has a predominantly O 2p character. The conduction band consists mainly of Ti 3d orbitals, with widths of about 2.5 eV. Ti $3d_{z^2}$ orbital character is predominant at the bottom of the conduction band (Figures 2a and 3). Experimentally, 4H-$BaTiO_3$ has been shown to be an n-type semiconductor[45] in which the electron-carrier concentration can be tuned by altering the oxygen deficiency or by substituting a trivalent cation at the $Ba^{2+}$ site or a pentavalent cation at the $Ti^{4+}$ site. In undoped 4H-$BaTiO_3$, the Fermi level may be located about several tens to several hundreds of millielectronvolts below the bottom of the conduction band as well as $SrTiO_3$[46].

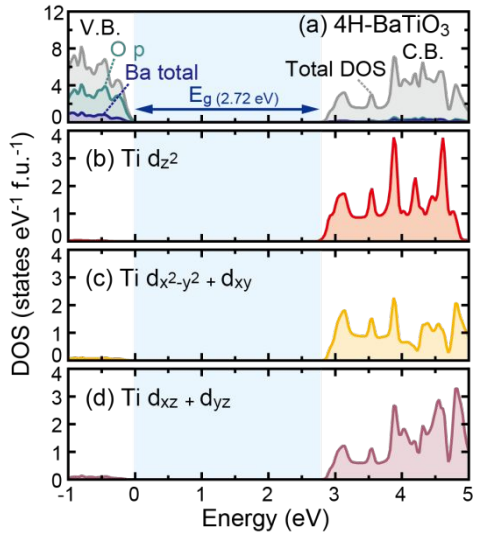


**Figure 3.** Total and partial density of states (DOS) in 4H-hexagonal perovskite $BaTiO_3$. (a) Total and partial DOSs of Ba and O 2p, (b) Ti $d_{z^2}$, (c) Ti $d_{x^2-y^2}$ + $d_{xy}$, and (d) Ti $d_{xz}$ + $d_{yz}$ orbitals. These DOSs were calculated by using the mBJ exchange potential.

On the other hand, the electronic structures of the 2H-type hexagonal perovskites $BaTiS_3$ and $SrTiS_3$ calculated by using the GGA-PBE functional or the mBJ exchange potential do not show energy band gaps unless on-site Coulomb interactions are considered. Energy band gaps in 2H-$BaTiS_3$ and $SrTiS_3$ appear in the electronic structures as calculated by the GGA-PBE+*U* method in which an effective on-site Coulomb interaction $U_{eff}$

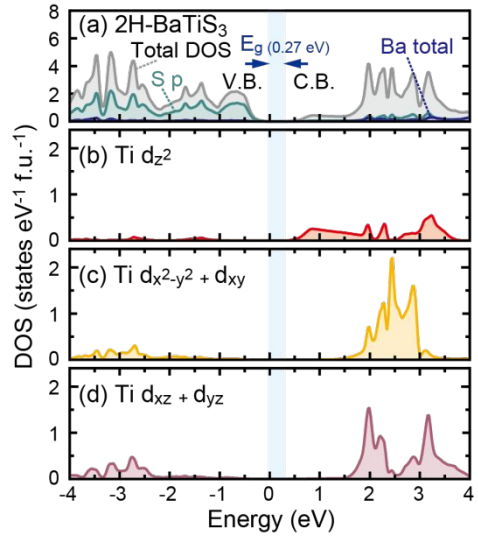


**Figure 4.** Total and partial density of states (DOS) in 2H-hexagonal perovskite $BaTiS_3$. (a) Total and partial DOSs of Ba and S 2p, (b) Ti $d_{z^2}$, (c) Ti $d_{x^2-y^2}$ + $d_{xy}$, and (d) Ti $d_{xz}$ + $d_{yz}$ orbitals. These DOSs were calculated by the GGA-PBE+*U* method ($U_{eff}$ = 8 eV).

was taken into account for the Ti site ($U_{eff}$ > 6 eV for $BaTiS_3$; $U_{eff}$ > 8 eV for $SrTiS_3$) (Figures 2c and S2). These results are consistent with those of previous DFT calculations using hybrid HSE06 functional.[43] The calculated energy band gaps (direct) at the Γ-points are 0.27 eV for 2H-$BaTiS_3$ ($U_{eff}$ = 8 eV) and 0.18 eV for 2H-$SrTiS_3$ ($U_{eff}$ = 9 eV). The energy band gaps therefore differ depending on the value of $U_{eff}$. As in the case of 4H-$BaTiO_3$, the lowest conduction bands and the highest valence bands in 2H-$BaTiS_3$ and $SrTiS_3$ have Ti 3d and S 3p orbital characters, respectively (Figure 4). The Ti 3d orbital characters in the conduction bands extend through a range of 4 eV from the bottom of the condition bands (Figures 4 and S3).

The crystal field splitting d orbital energies of face-sharing octahedra differ from those of corner-sharing octahedra, as recently described by the groups of Khomskii and Rondinelli.[47,48] In corner-sharing octahedra, triply degenerate $t_{2g}$ ($d_{xy}$, $d_{yz}$, $d_{xz}$) and doubly degenerate $e_g$ ($d_{x^2-y^2}$, $d_{z^2}$) energy levels are observed. In contrast, the $t_{2g}$ orbital levels of a face-sharing transition-metal ion are further split into a lowest energy level of a singlet $a_{1g}$ ($d_{z^2}$) and a doubly degenerate $e^{\pi}_g$ energy level ( $-\frac{2}{\sqrt{6}}d_{xy}+\frac{2}{\sqrt{3}}d_{yz}$, $\frac{2}{\sqrt{6}}d_{x^2-y^2}+\frac{1}{\sqrt{3}}d_{xz}$) due to a trigonal distortion of the anion octahedra and electrostatic interactions from nearby transition-metal cations. The other $e^{\sigma}_g$ energy level ($\frac{1}{\sqrt{3}}d_{x^2-y^2}-\sqrt{\frac{2}{3}}d_{xz}$, $-\frac{1}{\sqrt{3}}d_{xy}-\sqrt{\frac{2}{3}}d_{yz}$) is formed as the highest energy level located above the singlet $d_{z^2}$ ($a_{1g}$) orbital energy level and the doubly degenerate $e^{\pi}_g$ energy level. In 4H-$BaTiO_3$, 2H-$BaTiS_3$, and $SrTiS_3$, which consist of face-sharing octahedra, the Ti $3d_{z^2}$ ($a_{1g}$) orbital character is dominant in the lowest conduction bands, except for the L–H directions, as shown in Figure 2. Figures 2b, 2d, and S2b show the orbital characteristics of the lowest conduction bands. Ti $3d_{x^2-y^2}$ + $3d_{xy}$ orbital characters are dominant in the L–H directions of the electronic band structures of 4H-$BaTiO_3$, 2H-$BaTiS_3$, and $SrTiS_3$. In agreement with the description given by Khomskii et al., the lowest energy levels of the Ti $3d_{z^2}$ ($a_{1g}$) orbitals in 4H-$BaTiO_3$, 2H-$BaTiS_3$, and $SrTiS_3$ are located at the bottoms of conduction bands of Γ-points, because there are fewer contributions to the valence bands from Ti 3d orbitals. The Ti–X (X = O, S) bond lengths in face-sharing octahedra are 1.983 Å for 4H-$BaTiO_3$,[21] 2.424 Å for 2H-$BaTiS_3$,[22] and 2.372 Å for 2H-$SrTiS_3$.[23] The electronic structures are not affected by octahedral distortions, because there are no variations in the Ti–X (X = O, S) bond lengths in 4H-$BaTiO_3$, 2H-$BaTiS_3$, and $SrTiS_3$.

### Edge-sharing octahedra in $d^0$-layered complex metal nitrides $AMN_2$ with an α-$NaFeO_2$-type crystal structure

α-$NaFeO_2$-type and other related layered crystal structures consisting of edge-sharing octahedral layers (Figure 1c) have important applications in energy generation and energy saving. For example, $Na_xCoO_2$ has excellent thermoelectric properties[7] and is a base material for superconductors,[3] whereas $LiCoO_2$ is used as a cathode material in lithium-ion batteries.[49] To compare the d-orbital characters of face-sharing octahedra and edge-sharing trigonal prismatic layers with those of edge-sharing octahedra, we studied the electronic structures of several $d^0$-layered complex metal nitride $AMN_2$ (A = $Na^{1+}$, $Sr^{2+}$; M = $Nb^{5+}$, $Ta^{5+}$, $Zr^{4+}$, $Hf^{4+}$) with an α-$NaFeO_2$-type crystal structure. The electronic structures of $SrZrN_2$, $SrHfN_2$, $NaNbN_2$, and $NaTaN_2$, which have an α-$NaFeO_2$-type crystal structure, have been previously evaluated by DFT calculations.[50–53] All four of these α-$NaFeO_2$-type $d^0$-$AMN_2$ compounds are band insulators with energy-band gaps of 1.29 eV for $SrZrN_2$, 1.37 eV for $SrHfN_2$, 1.53 eV for $NaNbN_2$, and 2.19 eV for $NaTaN_2$, as calculated by using the mBJ exchange potential. Calculations using the mBJ exchange potential showed that the principal

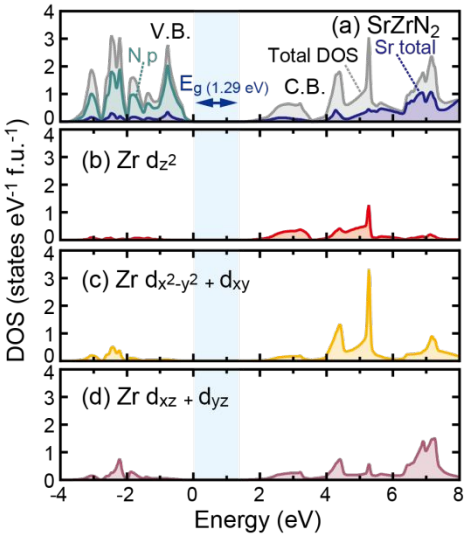


**Figure 5.** Total and partial density of states (DOS) in α-$NaFeO_2$-type $SrZrN_2$. (a) Total and partial DOSs of Sr and N 2p, (b) Zr $d_{z^2}$, (c) Zr $d_{x^2-y^2}$ + $d_{xy}$, and (d) Zr $d_{xz}$ + $d_{yz}$ orbitals. These DOSs were calculated by using the mBJ exchange potential.

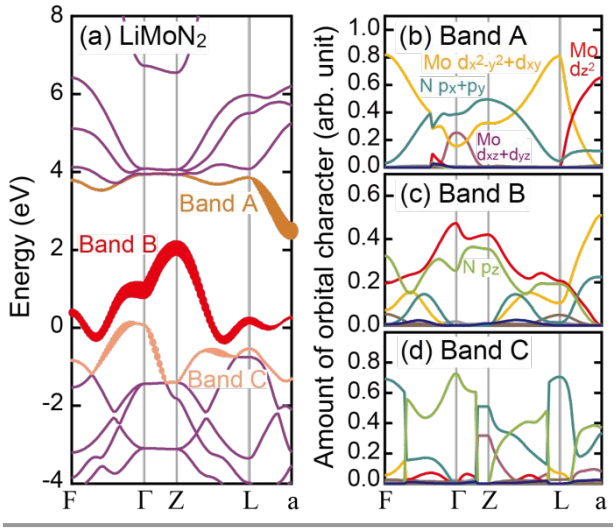


**Figure 6.** (a) Electronic band structure and (b)–(d) orbital characters for the electronic bands (Bands A–C, respectively) near the Fermi level in $LiMoN_2$. The amount of Mo $4d_{z^2}$ orbital character is shown by the width of the line in the band structure (Bands A–C near the Fermi level). All s orbitals, p orbitals ($p_z$, $p_x$ + $p_y$ for Mo; $p_x$, $p_y$, $p_z$ for N), and d orbitals ($d_{z^2}$, $d_{x^2-y^2}$ + $d_{xy}$, $d_{xz}$ + $d_{yz}$ for Mo) are plotted in Figures 6b, 6c, and 6d. The electronic band structure was calculated by using the GGA-PBE functional.

contributors to the valence bands and the conduction bands of these four α-$NaFeO_2$-type $AMN_2$ are the N 2p orbitals and M-site d orbitals, respectively (Figures 5 and S4). This is similar to the case in other $d^0$-ionic transition-metal compounds, such as $BaTiO_3$. The d orbitals of each M-site are the major contributors to the lowest conduction bands of the four $AMN_2$ compounds that we examined. At the bottom of the conduction bands (F-points) in $SrZrN_2$,[50] $SrHfN_2$,[50] $NaNbN_2$,[53] and $NaTaN_2$,[53] the $d_{z^2}$ orbital characters of the transition metal (Zr, Hf, Nb, or Ta) are predominant. Octahedral distortion has no effect on the electronic structures of our four α-$NaFeO_2$-type $AMN_2$ compounds, because there are no M–N bond-length distributions.[24–26]

**Edge-sharing trigonal prismatic layers in $d^1$-layered complex metal nitrides $LiMN_2$ (M = Mo or W)**

Lithium-metal-containing layered compounds have attracted a great deal of attention as materials for lithium-ion batteries. $LiMoN_2$ and $LiWN_2$ are $d^1$-layered complex transition-metal compounds composed of edge-sharing $MoN_6$ or $WN_6$ trigonal prismatic layers, as shown in Figure 1d.[27,28] The electrochemical properties of $LiMoN_2$ and $LiWN_2$ were also evaluated. Figures 6 and S5 show the electronic band structures of $LiMoN_2$ and $LiWN_2$, respectively, and 7 and S6 show the corresponding densities of states (DOSs). We evaluated the electronic structures of $LiMoN_2$ and $LiWN_2$ by using the GGA-PBE functional without considering the on-site Coulomb interaction ($U_{eff}$). In both $LiMoN_2$ and $LiWN_2$, the Fermi (zero-energy) levels include several electronic bands and DOSs but no energy band gaps, indicating the presence of three-dimensional metallic electronic structures. These metallic electronic structures are produced by $Mo^{5+}(4d^1)$ or $W^{5+}(5d^1)$ atoms in prismatic coordination. Differences in electronic structures between octahedral and prismatic metal coordination have been discussed by Hoffmann and co-workers.[54,55] These results are consistent with those of previous DFT calculations.[56,57] The results of calculations using the mBJ exchange potential and the GGA-PBE+$U$ approach ($U_{eff}$ ≈ 9 eV for Mo and W) also showed the presence of similar three-dimensional metallic electronic structures. The orbital characters of electronic bands and the partial DOS behaviors of d orbitals near the Fermi levels are rather complicated. As shown in Figure 6a, two electronic bands (Bands B and C) with Mo d-orbital character cross the Fermi level in $LiMoN_2$. The predominant orbital character is Mo $4d_{z^2}$ in the F–Γ–Z–L direction of Band B, located near the Fermi level (Figure 6c). At the F- and a-points of Band B, N $2p_z$ and Mo $4d_{x^2-y^2}$ + $4d_{xy}$ orbital characters are dominant, respectively. In addition to the Mo $4d_{z^2}$ orbital, N $2p_z$ orbitals also make a significant contribution to Band B, indicating hybridization of Mo $4d_{z^2}$ and N $2p_z$ orbitals around the Fermi level. In contrast, the main contributors to Band C, located at a lower energy level to Band B, are N 2p orbitals; Mo 4d orbitals make few contributions to Band C. The electronic band Band A is located in the range 2 to 4 eV (Figure 6a); its main contributors are the Mo $4d_{z^2}$ orbital at the a-point, the Mo $4d_{x^2-y^2}$ + $4d_{xy}$ orbitals at the F- and L-points, and the N $2p_x$ + $2p_y$ orbitals in the direction Γ–Z. Band A mainly contains Mo $4d_{z^2}$ and $4d_{x^2-y^2}$ + $4d_{xy}$ orbital characters, although it does not intersect with Band B and is separated from Band B and from the Fermi level. Therefore, as shown in the partial DOSs of the Mo $d_{z^2}$ and $d_{x^2-y^2}$ + $d_{xy}$ orbitals (Figures 7b and 7c), significant contributions of Mo $4d_{z^2}$ and $4d_{x^2-y^2}$ + $4d_{xy}$ orbital characters appear separately near the Fermi level (0 eV) and at about 3–4 eV, corresponding to the locations of Bands A and B. N 2p orbitals also contribute to the electronic bands near the Fermi level and at about 3–4 eV, as shown in Figure 7. This fact indicates that hybridized orbital characters combining Mo $4d_{z^2}$ and $4d_{x^2-y^2}$ + $4d_{xy}$ with N 2p appear in Bands A and B.

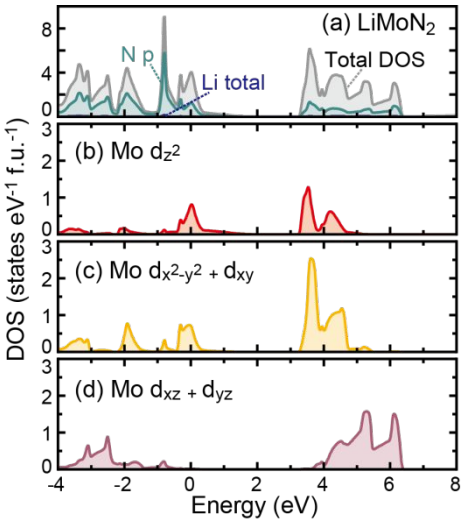


**Figure 7.** Total and partial density of states (DOS) in $LiMoN_2$. (a) Total and partial DOSs of Li and N 2p, (b) Mo $d_{z^2}$, (c) Mo $d_{x^2-y^2} + d_{xy}$, and (d) Mo $d_{xz} + d_{yz}$ orbitals. The DOSs were calculated by using the GGA-PBE functional.

The electronic band characters in $LiWN_2$ show a similar trend to those of $LiMoN_2$ (Figures S5 and S6). In $LiWN_2$, three electronic bands (Bands C, D, and E in Figure S5) cross the Fermi level (0 eV). The predominant orbital characters are W $5d_{x^2-y^2} + 5d_{xy}$ on the Fermi level near the K- and H-points, and W $5d_{z^2}$ below the Fermi level near the Γ- and A-points in Bands C and D. In Band E, the contribution of N 2p orbitals is dominant. In Bands A and B, located in the range between 3 and 5 eV, the predominant orbital characters are W $5d_{z^2}$ near the K- and H-points, and W $5d_{x^2-y^2} + 5d_{xy}$ in the Γ-A direction near the K-point. The DOS in $LiWN_2$ (Figure S6) shows that large contributions of W $5d_{z^2}$ and $5d_{x^2-y^2} + 5d_{xy}$ orbital characters are separately present near the Fermi level (0 eV) and at about 4 eV, corresponding to the locations of Bands C and D near the Fermi level and Bands A and B at about 4 eV. The electronic bands near the Fermi level and at about 4 eV also contain N 2p orbital character, as shown in Figure S6. Hybridized orbital characters of W $5d_{z^2}$, $5d_{x^2-y^2} + 5d_{xy}$ and N 2p are also present near the Fermi level and at about 4 eV. This trend is similar to that displayed by $LiMoN_2$.

According to crystal field theory, in a trigonal prismatic geometry the electron d orbital levels are split into a lowest energy level of a singlet $a_2$ ($d_{z^2}$), a doubly degenerate $e_2$ middle energy level ($d_{x^2-y^2}$, $d_{xy}$), and a highest energy level of doubly degenerate $e_3$ ($d_{xz}$, $d_{yz}$).[13] However, in $LiMoN_2$, the lowest Mo 4d orbital character is $4d_{xz} + 4d_{yz}$, located in the range –4 to –1 eV, as shown in Figure 7. This is inconsistent with crystal field theory, probably as a result of the limitations of this theory in solids. One possible reason is the effect of the formation of electronic bands containing hybridized orbital characters of Mo 4d and N 2p in $LiMoN_2$. Another possible reason is the effect of trigonal prismatic distortion. There are two different Mo–N bond lengths of 2.091 Å and 2.096 Å in $LiMoN_2$.[27] Slight structural distortion induced by these two different Mo–N bond lengths might also account for the difference between the description provided by crystal field theory and the results of DFT electronic structure calculations.

## Conclusions

The electronic structures of $d^0$- and $d^1$-complex transition-metal compounds containing various types of polyhedra were calculated. In the 4H-type hexagonal perovskite $BaTiO_3$ and the 2H-type hexagonal perovskites $BaTiS_3$ and $SrTiS_3$ ($d^0$-semiconductors), consisting of face-sharing $TiX_6$ (X = O, S) octahedral blocks, Ti $3d_{z^2}$ orbital characters predominate near the bottom of conduction bands; this is consistent with the description provided by crystal field theory. Similar tendencies were found in the $d^0$-layered complex metal nitrides $AMN_2$ with an α-$NaFeO_2$-type crystal structure containing edge-sharing $MN_6$ octahedral layers. In these compounds, the $d_{z^2}$ orbital characters of transition metals at the M-site are the main contributors to the bottom of the conduction bands. In contrast, in $LiMoN_2$ and $LiWN_2$ ($d^1$-transition metals) composed of $MoN_6$ or $WN_6$ edge-sharing trigonal prismatic layers, Mo (or W) $d_{z^2}$ and $d_{x^2-y^2} + d_{xy}$ orbital characters separately contribute to two different bands near the Fermi levels. Significantly large contributions of $d_{z^2}$ orbitals to the electronic bands near the Fermi levels are found in nine different complex transition-metal compounds consisting of either face-sharing octahedra, edge-sharing octahedra, or edge-sharing trigonal prismatic layers. In ionic transition-metal compounds, many physical and chemical properties result from the presence near the Fermi levels of electronic bands that contain contributions from d orbitals of the transition metal. Control of the $d_{z^2}$ orbital characters of transition metal is considered vital in relation to the exploration of novel physical and chemical properties, including various semiconducting properties, thermoelectric transport properties, anomalous metallic/semimetallic states, magnetism, electrocatalytic oxygen-evolution reactions, and catalytic activity, of complex transition-metal compounds.

## Conflicts of interest

There are no conflicts to declare.

## Acknowledgements

This work was supported by JST-PRESTO (JPMJPR15N1), the *Materials Research by Information Integration* Initiative ($MI^2I$) project of the Support Program for Starting Up Innovation Hub by JST, the JST-Mirai Program (JPMJMI18G5), the Kazuchika Okura Memorial Foundation, and JSPS KAKENHI (JP16H064xx).

## References

1 J. G. Bednorz and K. A. Muller, *Z. Phys. B* 1986, **64**, 189.
2 S. Yamanaka, K. Hotehama, and H. Kawaji, *Nature* 1998, **392**, 580–582.
3 K. Takada, H. Sakurai, E. Takayama-Muromachi, F. Izumi, R. A. Dilanian, and T. Sasaki, *Nature* 2003, **422**, 53–55.
4 Y. Kamihara, T. Watanabe, M. Hirano, and H. Hosono, *J. Am. Chem. Soc.* 2008, **130**, 3296–3297.
5 C. N. R. Rao and B. Raveau, *Transition Metal Oxides: Structure, Properties, and Synthesis of Ceramic Oxides*, Second edition, A John Wiley & Sons, INC., Publication: Hoboken, NJ, 1998.

6 S. V. Streltsov and D. I. Khomskii, *Proc. Natl. Acad. Sci. U.S.A.* 2016, **113**, 10491−10496.
7 I. Terasaki, Y. Sasago, and K. Uchinokura, *Phys. Rev. B: Condens. Matter,* 1997, **56**, R12685–R12687.
8 J. Son, P. Moetakef, B. Jalan, O. Bierwagen, N. J. Wright, R. Engel-Herbert, and S. Stemmer, *Nat. Mater.* 2010, **9**, 482−484.
9 B. Radisavljevic, A. Radenovic, J. Brivio, V. Giacometti, and A. Kis, *Nat. Nanotechnol.* 2011, **6**, 147–50.
10 K. P. Ong, D. J. Singh, and P. Wu, *Phys. Rev. Lett.* 2010, **104**, 176601.
11 Y. Lu, F. Lu, Z. Yang, J. Wu, H. Yu, X. Xie, J. Xu, F. Cheng, J. Chen, K. Xiong, H. Liu, W-H. Wang, J. Zhao, and W. Wang, *AIP Adv.* 2016, **6**, 095210.
12 D. Er, H. Ye, N. C. Frey, H. Kumar, J. Lou, and V. B. Shenoy, *Nano Lett.* 2018, **18**, 3943−3949.
13 I. B. Bersuker, *Electronic Structure and Properties of Transition Metal Compounds: Introduction to the Theory*, Second edition, A John Wiley & Sons, INC., Publication: Hoboken, NJ, 2010.
14 S. Y. Istomin, J. Köhler, and A. Simon, *Physica C* 1999, **319**, 219–228.
15 P. Wissgott, A. Toschi, H. Usui, K. Kuroki, and K. Held, *Phys. Rev. B: Condens. Matter,* 2010, **82**, 201106(R).
16 H. Sakakibara, H. Usui, K. Kuroki, R. Arita, and H. Aoki, *J. Phys.: Conf. Ser.* 2012, **400**, 022100.
17 G. J. Shu and F. C. Chou, *Phys. Rev. B: Condens. Matter,* 2013, **88**, 155130.
18 C. Gong, H. Zhang, W. Wang, L. Colombo, R. M. Wallace, and K. Cho, *Appl. Phys. Lett.* 2013, **103**, 053513.
19 G.-B. Liu, D. Xiao, Y. Yao, X. Xude, and W. Yao, *Chem. Soc. Rev.* 2015, **44**, 2643–2663.
20 X. Yao, J. Liu, W. Wang, F. Lu, and W. Wang, *J. Chem. Phys.* 2017, **146**, 224703.
21 J. Akimoto, Y. Gotoh, and Y. Oosawa, *Acta Cryst.* 1994, **C50**, 160–161.
22 J. Huster, *Z. Naturforsch. B,* 1980, **35**, 775.
23 H. Hahn and U. Mutschke, *Zeitschrift fuer Anorganische und Allgemeine Chemie* 1956, **288**, 269–278.
24 D. H. Gregory, M. G. Barker, P. P. Edwards, and D. J. Siddons, *Inorg. Chem.* 1996, **35**, 7608–7613.
25 H. Jacobs and B. Hellmann, *J. Alloys Compd.* 1993, **191**, 51–52.
26 H. Jacobs and E. von Pinkowski, *J. Less-Common Met.* 1989, **146**, 147–160.
27 S. H. Elder, L. H. Doerrer, F. J. DiSalvo, J. B. Parise, D. Guyomard, and J. M. Tarascon, *Chem. Mater.* 1992, **4**, 929–937.
28 S. Kaskel, D. Hohlwein, and J. Strähle, *J. Solid State Chem.* 1998, **138**, 154–159.
29 V. Grasso, *Electronic Structure and Electronic Transitions in Layered Materials*, D. Reidel Publishing Company, Dordrecht, 1986.
30 P. Blaha, K. Schwarz, G. Madsen, D. Kvasicka, and J. Luitz, *WIEN2k, An Augmented Plane Wave + Local Orbitals Program for Calculating Crystal Properties*; TU Vienna: Vienna, Austria, 2001.
31 F. Tran and P. Blaha, *Phys. Rev. Lett.* 2009, **102**, 226401.
32 D. Koller, F. Tran, and P. Blaha, *Phys. Rev. B: Condens. Matter,* 2011, **83**, 195134.
33 J. P. Perdew, K. Burke, and M. Ernzerhof, *Phys. Rev. Lett.* 1996, **77**, 3865–3868.
34 J. P. Perdew, K. Burke, and M. Ernzerhof, *Phys. Rev. Lett.* 1997, **78**, 1396.
35 K. Momma and F. Izumi, *J. Appl. Crystallogr.* 2011, **44**, 1272−1276.
36 V. M. Goldschmidt, *Naturwissenschaften* 1926, **14**, 477–485.
37 J. T. Rijssenbeek, R. Jin, Y. Zadorozhny, Y. Liu, B. Batlogg, and R. J. Cava, *Phys. Rev. B: Condens. Matter,* 1999, **59**, 4561–4564.
38 R. A. Gardner, M. Vlasse, and A. Wold, *Acta Cryst.* 1969, **B25**, 781–787.
39 N. Nakamura, A. Sekiyama, H. Namatame, A. Fujimori, H. Yoshida, T. Ohtani, A. Misu, and M. Takano, *Phys. Rev. B: Condens. Matter,* 1994, **49**, 16191–16201.
40 I. Terasaki, S. Ito, T. Igarashi, S. Asai, H. Taniguchi, R. Okazaki, Y. Yasui, K. Kobayashi, R. Kumai, H. Nakao, and Y. Murakami, *Crystals* 2016, **6**, 27.
41 Y. Akishige, G. Oomi, T. Yamamoto, and E. Sawaguchi, *J. Phys. Soc. Jpn.* 1989, **58**, 930–939.
42 J. Yu, P.-F. Paradis, T. Ishikawa, S. Yoda, Y. Saita, M. Itoh, and F. Kano, *Chem. Mater.* 2004, **16**, 3973–3975.
43 Yi-Y. Sun, M. L. Agiorgousis, P. Zhang, and S. Zhang, *Nano Lett.* 2015, **15**, 581−585.
44 Y. Akishige, *J. Phys. Soc. Jpn.* 1995, **64**, 4033–4037.
45 D. C. Sinclair, J. M. S. Skakle, F. D. Morrison, R. I. Smith, and T. P. Bealesc, *J. Mater. Chem.* 1999, **9**, 1327–1331.
46 J. Robertson, *J. Vac. Sci. Technol., B: Microelectron. Nanometer Struct.–Process., Meas., Phenom.* 2000, **18**, 1785–1791.
47 D. I. Khomskii, K. I. Kugel, A. O. Boychakov, and S. V. Streltsovc, *J. Exp. Theor. Phys.* 2016, **122**, 484–498.
48 N. Wagner, R. Seshadri, and J. M. Rondinelli, *Phys. Rev. B: Condens. Matter,* 2019, **100**, 064101.
49 K. Mizushima, P. C. Jones, P. J. Wiseman, and J. B. Goodenough, *Mater. Res. Bull.* 1980, **15**, 783–789.
50 I. Ohkubo and T. Mori, *Inorg. Chem.* 2014, **53**, 8979–8984.
51 I. Ohkubo and T. Mori, *Eur. J. Inorg. Chem.* 2015, 3715–3722.
52 I. Ohkubo and T. Mori, *Chem. Mater.* 2015, **27**, 7265−7275.
53 I. Ohkubo and T. Mori, *APL Mater.* 2016, **4**, 104808.
54 M. Kertesz and R. Hoffmann, *J. Am. Chem. Soc.* 1984, **106**, 3453−3460.
55 R. Hoffmann, J. M. Howell, and A. R. Rossi, *J. Am. Chem. Soc.* 1976, **98**, 2484–2492.
56 D. J. Singh, *Phys. Rev. B: Condens. Matter,* 1992, **45**, 9332−9335.
57 J. M. Oliva, R. Weht, P. Ordejón, and E. Canadell, *Phys. Rev. B: Condens. Matter,* 2000, **62**, 1512−1515.

 

**Manuscript type**: Paper

# $d_{z^2}$ Orbital character of polyhedra in complex solid-state transition-metal compounds

*Isao Ohkubo*[*,a,b,c] *and Takao Mori*[a,b]

[a]Center for Functional Sensor & Actuator (CFSN), Research Center for Functional Materials, National Institute for Materials Science (NIMS), 1-1 Namiki, Tsukuba, Ibaraki 305-0044, Japan

[b]International Center for Materials Nanoarchitectonics (MANA), National Institute for Materials Science (NIMS), 1-1 Namiki, Tsukuba, Ibaraki 305-0044, Japan

[c]Center for Materials Research by Information Integration (CMI[2]), Research and Services Division of Materials Data and Integrated System (MaDIS), National Institute for Materials Science (NIMS), 1-1 Namiki, Tsukuba, Ibaraki 305-0044, Japan

[*]Corresponding author, e-mail address: OHKUBO.Isao@nims.go.jp

## Table of Contents Entry

$d_{z^2}$ Orbitals of the transition metals make major contributions to the electronic structures near the Fermi levels in $d^0$-, $d^1$-complex transition-metal compounds containing face-sharing, edge-sharing octahedra, or edge-sharing trigonal prismatic layers.